DOI:
10.1002/mrm.28178

Document Version
Peer reviewed version

FULL PAPER

Silent T_1 Mapping Using the Variable Flip Angle Method with B_1 Correction

Emil Ljungberg[1]* | Tobias Wood[1] | Ana Beatriz Solana[2] | Shannon Kolind[3,4,5,6] | Steven C.R. Williams[1] | Florian Wiesinger[†1,2] | Gareth J. Barker[†1]

[1]Department of Neuroimaging, Institute of Psychiatry, Psychology & Neuroscience, King's College London, London, UK

[2]ASL Europe, General Electric Healthcare, Munich, Germany

[3]Department of Physics and Astronomy, University of British Columbia, Vancouver Canada

[4]Department of Radiology, University of British Columbia, Vancouver, Canada

[5]International Collaboration on Repair Discoveries, University of British Columbia, Vancouver, Canada

[6]Medicine (Neurology), University of British Columbia, Vancouver, Canada

[†]Authors contributed equally to this work

Correspondence
Emil Ljungberg, Department of Neuroimaging, Institute of Psychiatry, Psychology & Neuroscience, King's College London, London, UK
Email: emil.ljungberg@kcl.ac.uk

Present address
*Centre for Neuroimaging Sciences, Institute of Psychiatry (PO89), De Crespigny Park, London SE5 8AF, United Kingdom

Funding information
The National Institute for Health Research (NIHR) Wellcome Trust King's Clinical Research Facility; NIHR Biomedical Research Centre at South London and Maudsley NHS Foundation Trust and King's College London; Wellcome/EPSRC Centre for Medical Engineering [WT 203148/Z/16/Z]; General Electric Healthcare

Purpose: To compare the silent Rotating Ultra-Fast Imaging Sequence (RUFIS) to a traditional Cartesian spoild gradient-echo (SPGR) acquisition scheme for Variable Flip Angle (VFA) T_1 mapping.

Method: A two point VFA measurement was performed using RUFIS and Cartesian SPGR in a quantitative phantom and healthy volunteers. To correct for B_1 errors, a novel Silent Magnetisation Prepared B_1 map Acquisition (SIMBA) was developed, which combined with RUFIS VFA allows for a completely silent T_1 mapping protocol.

Results: The silent protocol was found to have comparable repeatability but higher reproducibility in vivo compared to the standard SPGR protocol, and showed no increase in acoustic noise levels above background noise levels compared to a 33 dBA increase for the SPGR acquisition.

Conclusion: VFA T_1 mapping using RUFIS is a feasible alternative to SPGR, achieving silent T_1 mapping with comparable acquisition time.

Wordcount: 5230/5082 (including/excluding abstract)

KEYWORDS
T_1, Quantitative, MRI, Silent, ZTE

1 | INTRODUCTION

The variable flip angle method (VFA), also referred to as DESPOT1, is a method for T_1 estimation, originally proposed by Christensen and later adapted for imaging by Fram [1, 2, 3, 4, 5]. To obtain a T_1 estimate, two or more fully spoiled gradient echo images are acquired with varying excitation flip angles and linearly fitted to the signal equation [6]. Due to the use of a gradient-echo sequence and the low number of acquisitions required, the VFA method is highly efficient compared to inversion-recovery based methods [7]. However, due to the large phase-encoding and spoiler gradients and short TR typically used in clinical protocols, the VFA method produces loud acoustic noise which is a drawback for patient comfort. In addition, at modern field strengths of 3T and above, B_1 inhomogeneity becomes a significant issue that must be corrected for with a separate acquisition.

In this work, we present a method for VFA T_1 mapping using the 3D **R**otating **U**ltra-**F**ast **I**maging **S**equence (RUFIS)[8], which presents several potential advantages over a traditional Cartesian acquisition. First, because of the centre-out radial *k*-space trajectory and gradual change of the gradient direction between subsequent excitations, the acquisition is almost completely silent [9]. Secondly, the RUFIS sequence achieves an effective echo time of zero (ZTE) by performing RF excitation with the readout gradients on and directly acquiring the free induction decay (FID)[10]. This extends the limit of T_1 quantification to tissues with very short T_2 such as bone and lung tissue, which often are considered to be MR-invisible [11, 12].

We present theoretical signal equations for RUFIS and analyse the constraints imposed on the acquisition by the ZTE readout. The theory and implementation of a novel silent B_1^+ mapping technique, using an extension to the double angle method with a RUFIS readout, is also presented. The proposed silent T_1 and B_1^+ mapping techniques are demonstrated in a quantitative phantom with known relaxation characteristics and in vivo in four healthy volunteers, and compared to Cartesian methods.

2 | METHOD

2.1 | Theory - Quantitative RUFIS

An outline of the RUFIS pulse sequence diagram is shown in figure 1A. Each spoke is a single FID readout with a centre-out trajectory in k-space. The magnitude of the applied gradients remains the same, while the relative strength along each axis changes the direction of the spoke in k-space. The k-space trajectory is designed such that the endpoints of the spokes trace a spiral on the surface of a sphere in k-space, resulting in a near silent acquisition [9]. Data acquisition starts as soon as the system has switched from transmit to receive mode, resulting in an effective echo time of zero (ZTE). To achieve this, only ultra-short hard RF pulses with low flip angles can be used for excitation with RUFIS. Further more, the TR in RUFIS is only limited by the readout duration since no time is required for slice/slab and phase encoding gradients.

When a steady state has been reached with RUFIS, the acquired signal will be equivalent to that of a spoiled gradient echo sequence, with the signal intensity depending on T_1 and proton density ρ, as well as the repetition time (TR), and flip angle (α) as

$$M_{z,spgr} = \rho \cdot \frac{1 - e^{-TR/T_1}}{1 - \cos(\alpha) e^{-TR/T_1}}. \tag{1}$$

With RUFIS, only short TRs and low flip angles are used, and therefore a first order approximation of (1) can be

made [13, 14] as

$$M_{z,spgr} = \frac{\rho}{1 + \frac{T_1}{TR} \cdot \frac{\alpha^2}{2}}. \quad (2)$$

This assumes that the signal is fully spoiled between repetitions. In RUFIS, this is achieved with RF spoiling as well as gradient spoiling from the readout gradients.

To perform a T_1 measurement using the variable flip angle method (VFA), a minimum of two flip angles is required. Spatial variations in the B_1^+ field have to be measured independently since changes in T_1 and α cannot be separated in the signal equation, as seen in (2). In RUFIS, there are two sources of B_1^+ variation; dielectric effects, and excitation profile effects. The former is here addressed through development of a novel B_1^+ mapping technique using RUFIS (described in the next section), and the latter through an analytical correction.

The non-uniform excitation profile in RUFIS is caused by the readout gradient being present during RF excitation[15]. For a given spoke, the gradients alter the resonant frequency across the sample parallel to the spoke direction, resulting in an unwanted sinc-shaped spatial variation of the flip angle in the direction of the spoke. The excitation profile is determined by the product of the duration of the RF pulse (τ_{rf}) and readout gradient magnitude G (which is inversely proportional to the readout bandwidth) as

$$B_1^+(\bar{r}) = \mathrm{sinc}(\tau_{rf} \cdot \omega_G) \quad (3)$$

where $\omega_G = \gamma \cdot \bar{G} \cdot \bar{r}$, γ is the gyromagnetic ratio, and $\bar{G}$ and $\bar{r}$ are vectors describing the current gradient direction and the position in the sample, and $\max|\omega_G| = rBW$, i.e. the readout bandwidth.

In order to achieve a flat excitation profile, hard RF pulses with the shortest possible duration should be used. This requires using the maximum possible RF amplitude and choosing the duration of the RF pulse to be that required to achieve the highest flip angle desired. This introduces a practical upper limit of the maximum flip angle that can be achieved. Therefore, optimization of a RUFIS VFA T_1-mapping protocol has to consider a series of linked constraints. First, given a readout bandwidth the maximum excitation pulse width is limited to maintain an acceptable excitation profile; here we chose a limit of $\tau_{rf} \cdot rBW < 0.5$ which results in the excitation flip angle at the edge of the FoV falling to 63% of the prescribed flip angle. The chosen bandwidth will also determine the TR. The optimal flip angle sampling scheme in a VFA acquisition depends on the TR of the acquisition and the T_1 for which it is optimised [16]. With T_1 fixed, the optimal flip angles decrease with shorter TR. At the same time, a shorter TR, resulting from higher bandwidth, will also result in a shorter pulse width, and thus lower achievable flip angles. Tests on our scanner revealed that the pulse-width is the main limiting factor, and only at low bandwidths, here ±7.8 kHz can flip angles close to the optimal be achieved. However, the flip angle limitations might be different for different MR systems as they depend on the RF amplifier, coils and SAR constraints.

2.2 | Theory - B_1^+ mapping with RUFIS

The proposed B_1^+ mapping method uses a composite preparation pulse with different flip angles prior to a RUFIS readout to saturate the magnetisation proportional to the total flip angle, see figure 1B. We hereafter refer to this technique as SIMBA (**Si**lent **M**agnetisation prepared $\mathbf{B_1^+}$ **A**cquisition). To enable magnetisation preparation, the RUFIS readout is divided into segments with N spokes per segment. A series of n RF pulses with the same phase, flip angle α_{SAT}, and short inter-pulse spacing are applied as a preparation, acting as one composite pulse with effective flip angle $n \cdot \alpha_{SAT}$. The transverse magnetisation after preparation is spoiled using a spoiling gradient, resulting in an initial longitudinal

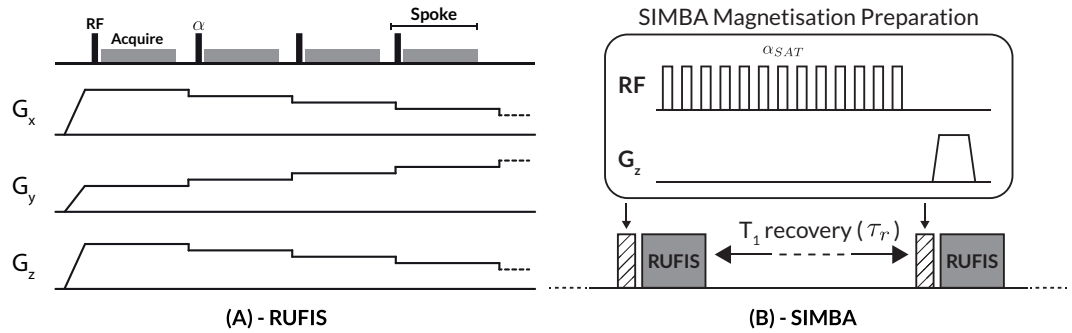

FIGURE 1 **(A)** Schematic pulse sequence diagram of the RUFIS sequence. Excitation is performed with an ultra-short hard RF pulse with the gradients on, and the free induction decay (FID) is acquired. The gradient magnitude stays the same and only the direction changes for each spoke. **(B)** Schematic of the SIMBA pulse sequence with the magnetisation preparation module before the RUFIS readout segment. A series of hard pulses with flip angle α_{SAT} is applied and the transverse magnetisation after the train of pulses is crushed with a gradient on the z axis. The delay τ_r between preparations allows for T_1 recovery.

magnetisation before readout given by $\tilde{M}_0 = \rho \cdot \cos(n\alpha_{SAT})$. To produce a B_1^+ mapping technique that is consistent with the RUFIS readout, ultra-short RF pulses are used in the preparation. Using similar pulses in the preparation as in the readout enables characterization of potential errors in the hard RF pulses, e.g. not reaching the peak amplitude instantaneously, as would be the case for a perfect rectangular pulse, which would result in a global, non-spatial, B_1^+ error.

The observed magnetisation in a RUFIS acquisition is proportional to the average magnetisation within a segment $\bar{M}_T(N)$ which can be expressed as

$$\bar{M}_T = \sin\alpha \cdot \bar{M}_z \tag{4}$$

$$\bar{M}_z = \tilde{M}_0 \cdot f + M_{z,spgr}(1-f) \tag{5}$$

$$f = \frac{1-\xi^N}{N(1-\xi)}, \quad \xi = \cos\alpha \cdot e^{-TR/T_1}. \tag{6}$$

where $\tilde{M}_0$ is the prepared longitudinal magnetisation at the beginning of the segment, and α is the excitation flip angle in the RUFIS readout. The full derivation of this expression can be found in the appendix. Encoding the B_1^+ efficiency as a factor λ, makes the transverse magnetisation proportional to λ as

$$\bar{M}_T = \left[\rho \cdot \cos(n \cdot \lambda \cdot \alpha_{SAT}) \cdot f + M_{z,spgr}(1-f)\right] \cdot \sin\alpha \tag{7}$$

assuming full T_1 recovery between preparations. Figure 2A shows how the prepared magnetisation changes with the total preparation flip angle ($n \cdot \alpha_{SAT}$) for $\lambda = (0.8, 1.0, 1.2)$. The repeated excitation in the RUFIS readout results in a positive offset in the signal, explained by the second term in (7), as shown in figure 2B. While increasing the number of spokes per segment will reduce the acquisition time, it will also reduce the dynamic range of the measurement.

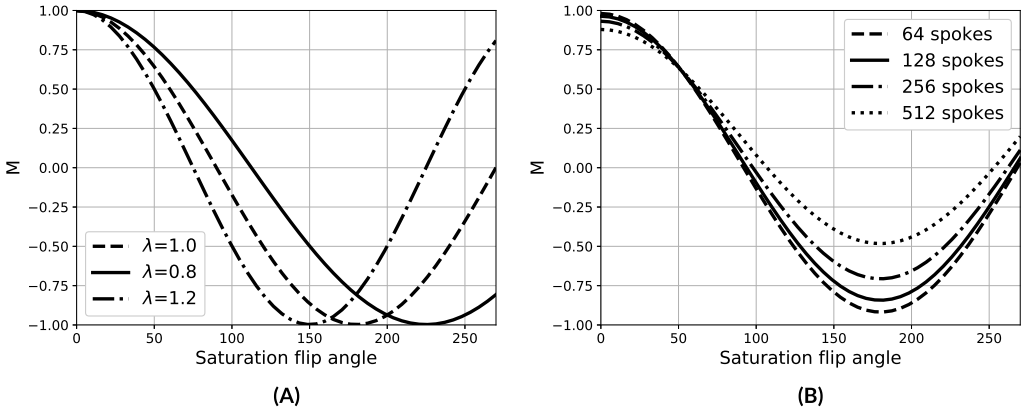

FIGURE 2 **(A)** Simulation showing the effect of B_1^+ efficiency (λ) on the prepared magnetisation. **(B)** Simulation showing the effect of the RUFIS readout on the prepared magnetisation assuming $\lambda = 1$, $T_1 = 1s$, RUFIS $\alpha = 2°$ and TR=1 ms.

2.3 | MR Acquisition

MR experiments were performed on a GE MR750 3T scanner (GE Healthcare, Chicago, IL) using the body coil for RF transmission and a 12-channel head RF receive coil. VFA T_1-mapping data were acquired with a 3D RUFIS sequence and a Cartesian SPGR sequence for comparison. The acquisitions were matched in field of view (FOV) (192x192x192 mm^3), voxel size (1.5x1.5x1.5 mm^3) and acquisition time. Because of the difference in TR between RUFIS and SPGR, a different set of flip angles (α) were acquired, to match the optimal set [16]. RUFIS data were acquired with α=2° & 12°, TR=4.4 ms, TE=0 ms, readout bandwidth=±7.8 kHz, 24576 readout spokes in total, RF spoiling phase increment=117.0°. The RF pulse width was fixed to 64 μs. The current implementation of the RUFIS sequence is restricted to a segmented readout to allow for magnetisation preparation such as T_1 and T_2 preparation, resulting in a delay of about 20 ms between segments to allow the gradients to be ramped down and up quietly. However, with a high number spokes per segment, here 512, the duration of the segment is approximately 2.25 s and the delay between segments is only 20 ms, therefore the delay does not alter the steady state substantially. Cartesian images were collected with α=3.5°& 20°, TR=10.6 ms, TE=3.4 ms, parallel imaging factor=1.5 (ASSET), RF spoiling increment=115.4°. Total acquisition time of the RUFIS and SPGR protocols was matched to ≈2 mins per flip angle, 4 mins total, in both cases.

Two sets of B_1^+ maps were acquired; Bloch-Siegert [17] for correcting the SPGR data, and SIMBA for RUFIS data. Bloch-Siegert data were acquired using a 2D multi-slice sequence with an 8 ms Fermi pulse applied 4 kHz off resonance, readout parmeters: FA=15°, TE/TR=13.1/18 ms, in-plane resolution=4x4 mm^2, FOV=256x256 mm^2, 40 slices with 4 mm slice thickness, duration=1:40 min. SIMBA data were acquired using the 3D RUFIS sequence with readout bandwidth=±9.25 kHz, α=1°, 6x6x6 mm^3 resolution, 192x192x192 mm^3 FOV, 256 spokes per segment, preparation α_{SAT}=5°, number of pulses in preparation train=[54,36,18,0], 3 s recovery time. Acquisition parameters were adjusted to achieve a total acquisition time of 1 minute. Each scanning session also included a sagittal T_1-weighted IR-SPGR (BRAVO) for tissue segmentation with TE/TR/TI=3/7/400 ms, FOV=270x270x240 mm^3, slice thickness=1.2 mm, in-plane resolution=1.05x1.05 mm^2, FA=11°, BW=31.25 kHz, and ASSET=1.75.

Four healthy volunteers were scanned twice with the same protocol, with an average time between scan sessions of 50 days (range: 48-52 days). In each session, the anatomical BRAVO image was acquired once and the VFA T_1-mapping

protocols using RUFIS and SPGR, with B_1^+ correction, were acquired twice (without repositioning). All scans were collected under ethical approval by the Camberwell St Giles NHS (National Health Service) HRA (Health Research Authority) Research Ethics Committee and participants gave written informed consent.

The protocol details above were also used to scan a quantitative phantom consisting of 12 vials with a range of T_1 values (T_1 =200-1500 ms, EUROSPIN test object 5 (TO5)[18]). Vials were mounted in an in-house made styrofoam mount. Due to the small size of the vials (≈2 cm in diameter), an additional SIMBA scan with higher resolution (4x4x4mm^3) was acquired for the phantom experiment. Increasing the resolution also increased the TR to 1.6 ms which was accounted for by reducing the number of spokes per segment to 176, to maintain the same T_1 recovery during the readout.

Acoustic noise measurements were performed using a Casella (IDEAL Industries, Ill) CEL-63X sound meter with an external microphone placed in the centre of the bore, mounted to a cylindrical water phantom with padding between the phantom and microphone to avoid vibrations. Measurements were taken throughout each of the scans with a sampling rate of 1 sample every 2 s. Within a 40 s segment for each sequence, the average A-weighted equivalent sound level (LAEQ [dBA]) and C-weighted peak sound level (LCPEAK [dBC]) were calculated.

2.4 | Image Reconstruction and Processing

Data acquired with RUFIS were reconstructed offline in MATLAB (MathWorks, Natick, MA, USA). Radial k-space data were gridded using the Kaiser-Bessel method. Coil sensitivity maps were estimated using ESPIRiT, implemented in the Berkeley Advanced Reconstruction Toolbox (BART) [19, 20, 21]. Images were reconstructed using a SENSE reconstruction with 3D Total Variation regularization with $\lambda = 0.001$ implemented in the `pics` command in BART. For SIMBA data, coil sensitivity maps were estimated from the centre of k-space using the method described by McKenzie et al., also implemented in BART [22].

To calculate the SIMBA B_1^+ map, real valued data is needed. Due to the effective TE=0 with RUFIS, no phase evolution is expected from the readout itself. The phase of the first image, with no preparation, was therefore subtracted from subsequent images, allowing positive signals to be distinguished from negative signals. The B_1^+ map was then calculated through a non-linear fit of the real data to the following equation

$$M = A \cdot \cos(\lambda \cdot n \cdot \alpha_{SAT}) + C. \tag{8}$$

To correct for the excitation profile in the RUFIS acquisition, an iterative simulation was performed where the excitation profile for individual spokes was calculated analytically using equation (3). The 3D excitation profile was calculated for 1024 spokes and then averaged. The simulated excitation profile was then multiplied by the SIMBA B_1^+ map to obtain a total B_1^+ correction.

Data acquired with RUFIS and SPGR were motion corrected using mcFLIRT[23]. B_1^+ maps from SIMBA and Bloch-Siegert were registered and transformed to the space of the associated VFA acquisition using an affine transformation [24]. The transformed B_1^+maps were smoothed using a Gaussian kernel with 8 mm FWHM to reduce propagation of noise into the T_1 maps. Quantitative T_1 and proton density maps were calculated using a linear fit, implemented in the QUantitative Imaging Tools (QUIT) [25]. The first RUFIS and SPGR acquisition within each scanning session were registered to the BRAVO scan using a combined affine and non-linear registration[26, 24]. A non-linear transformation was chosen as we observed minor differences in gradient distortions between the acquisitions, due to the different reconstruction pipelines used. The second VFA acquisition of each scanning session was registered to the first VFA acquisition using an affine transformation. This transformation was then combined with the non-linear transformation to the BRAVO image.

To obtain unbiased regions of interest (ROI) for analysis of the T_1-maps, the BRAVO data for each subject and each visit were segmented using Freesurfer [27]. The following ROIs from the FreeSurfer analysis were used in the analysis: Pallidum (ID: 13+52), Thalamus (ID: 10+49), Caudate (ID: 11+50), Putamen (ID: 12+51), Corpus Callosum (CC) posterior (ID: 255), CC anterior (ID: 251), cerebral white matter (WM) (ID: 2+41), cerebral cortex (ID: 3+42). FreeSurfer ROIs were warped to the native space of the VFA data using the previously calculated transformations in a single step with MultiLabel interpolation [24]. Average T_1 values were calculated within each ROI, bilateral ROIs were averaged. The image analysis pipelines were developed using the `nipype` framework [28].

2.5 | Statistical Analysis

Repeated scans within the same session were treated as measurements performed under identical conditions, defined as repeatability conditions [29], and analysed using the methods described by Bland and Altman[30]. Within each visit, each sequence, and each ROI, the mean ($\bar{d}$) and standard deviation (s_d) of the difference between repeated scans across the subjects were calculated. The coefficient of repeatability (CoR) was calculated as $CoR_w = 2s_d$, with subscript w indicating within visit. The CoR is an aggregate measure of the absolute variability in the data, i.e. it does not scale with the true T_1 within the ROI. Another value often reported in the literature is the coefficient of variation (CoV), this is calculated per subject as $CoV_w = 100 \cdot \text{std}(y_1, y_2)/\text{mean}(y_1, y_2)$ where y_1 and y_2 are the test-retest T_1 values within the same session. The CoV is a percentage estimate, which is scaled by the true T_1 inside the ROI. Since the CoV is defined in terms of a standard deviation, its statistical validity is limited when only a small number of measures are used to calculate it, and its value could be questioned in a study such as the current one with only two measurement points, results from CoV analysis are therefore only provided in the supporting information for comparison to the literature. Low CoR and CoV indicates high repeatability.

Repeated scans at the two different time points (i.e. visits), were treated as measurements taken under reproducibility conditions[29], with day-to-day biological variation and conditions in the scan room being factors not held constant. All other parameters were matched between the two scans. The within subject test-retest mean and difference in T_1 were utilized for the reproducibility analysis. The average difference between the test-retest values at each time point (D) and the standard deviation (s_D) across subjects were calculated. The corrected standard deviation of the mean of the differences was calculated as $s_c = \sqrt{s_D^2 + \frac{1}{4}s_{d,1}^2 + \frac{1}{4}s_{d,2}^2}$[30], where $s_{d,1}$ and $s_{d,2}$ are the standard deviation of the test-retest differences at the two time points. The coefficient of reproducibility was calculated as $CoR_b = 2s_c$, and the coefficient of variability as $CoV_b = 100 \cdot \text{std}(y_1, y_2)/\text{mean}(y_1, y_2)$ where y_1 and y_2 are the average T_1 values for visit 1 and 2 for each subject. Subscript b here indicates between visits.

Comparison of T_1 between the two sequences was performed using both in vivo and phantom data. With the in vivo data, whole brain histograms were calculated, and Bland-Altman plots of the isolated ROIs from all subjects were produced. Using the phantom data, Bland-Altman analysis was used to compare T_1 values within the individual vials.

3 | RESULTS

3.1 | B_1^+-mapping with SIMBA

The calculated B_1^+ map from SIMBA is shown in figure 3 along with the Bloch-Siegert B_1^+ map for comparison. The B_1^+ maps have been transformed to VFA space and smoothed as previously described. The B_1^+ field estimated by SIMBA was lower than Bloch-Siegert, a pattern that was also observed in the other subjects and in the repeated scans. Without any correction the RUFIS R_1 maps showed strong inhomogeneity around the edges of the brain, see 3 C. Applying B_1^+

correction to the RUFIS data with SIMBA and Bloch-Siegert showed similar improvements to the homogeneity in the R_1. However a shift in T_1 towards shorter values was observed when Bloch-Siegert was used for correcting RUFIS data, compared to using SIMBA, as shown in figure 3 D.

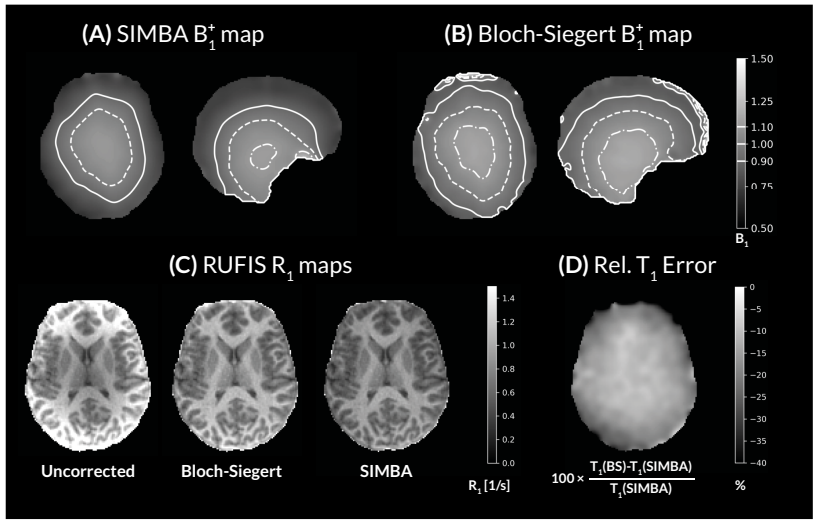

FIGURE 3 Comparison of B_1^+ maps acquired with SIMBA (A) and Bloch-Siegert shift (B). SIMBA produces slightly lower B_1^+ values, as seen by the contour lines. R_1 ($1/T_1$) maps calculated from RUFIS VFA data without B_1^+ correction show strong inhomogeneity (C). Applying SIMBA or Bloch-Siegert B_1^+ correction shows clear improvement. (D) Comparing T_1 maps from RUFIS with Bloch-Siegert and SIMBA B_1^+-correction shows a consistent shift towards lower T_1 values, with no obvious spatial variation, when Bloch-Siegert is used. (The R_1 map is shown instead of T_1 as it better highlights the effects of the B_1^+ correction.)

3.2 | T_1-mapping

An overview of the T_1 and PD maps from the first visit from RUFIS, with SIMBA B_1^+ correction, and SPGR, with Bloch-Sieger B_1^+ correction, is presented in figure 4. Qualitatively, the T_1 maps from RUFIS looked very similar to SPGR in the brain and the histograms, shown in 5, also overlap to a great extent. One noticable difference between the two acquisitions is outside the brain. The ZTE readout in RUFIS captures the short T_2 signal from the skull which can be seen clearly in the proton density and T_1 maps. The location of the WM peak in the T_1 histograms is similar between RUFIS and SPGR, with an average difference for the WM peak of $\Delta WM_{peak} = 70 \pm 40$ ms. However, a greater variability was observed for GM, $\Delta GM_{peak} = -180 \pm 70$ ms. This is also reflected in the Bland-Altman plot comparing T_1 values from RUFIS and SPGR within isolated ROIs presented in figure 6A, which shows larger difference for GM structures. Average T_1 values between the two repeated scans in the first visit, within isolated ROIs, are shown in table 1.

Similar results were observed in the phantom experiments. The RUFIS and SPGR T_1 values were found to be highly correlated (Pearson's $\rho = 0.93$), but Bland-Altman analysis (figure 6B) showed a trend for larger differences in T_1 between the two sequences for longer T_1, with an average difference in T_1 across all vials of $\bar{d} = -0.4$ s, and standard deviation of the mean of $s_d = 0.4$ s.

The average within session repeatability for all ROIs for the two visits were comparable between the two sequence;

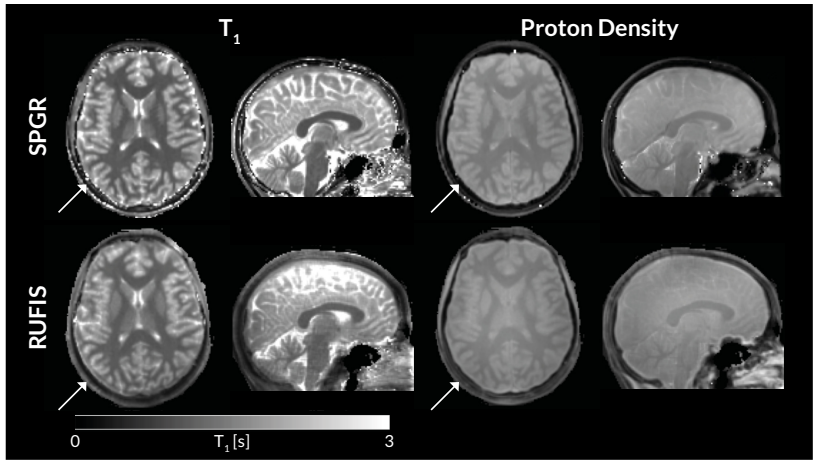

FIGURE 4 Example of quantitative T_1 and proton density maps from one subject acquired with RUFIS and Cartesian SPGR. Due to the ZTE readout in RUFIS, a T_1 fit could be obtained in the cortical bone, indicated by the white arrows, and a higher proton density was observed in the same area.

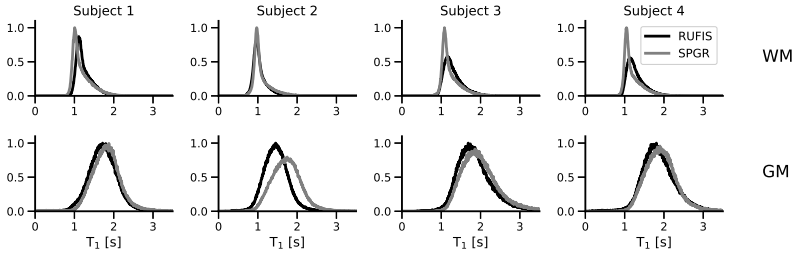

FIGURE 5 T_1-histograms of whole brain white matter and cortical gray matter from all four subjects from the first visit, averaged over the two scans.

RUFIS $CoR_{w,1}/CoR_{w,2} = 0.06/0.02$, SPGR $CoR_{w,1}/CoR_{w,2} = 0.05/0.08$. Better between sessions average reproducibility between all ROIs was found for RUFIS ($CoR_b = 0.07$) compared to SPGR ($CoR_b = 0.2$). Table 1 summarises the repeatability and reproducibility estimates from each individual ROI. The CoV values can be found in table S1 in the supporting information.

3.3 | Acoustic Noise Measurements

Table 2 shows average LAeq and LCpeak values from the acquisitions used in the protocol along with the ambient noise level in the scan room. RUFIS showed no measurable increase in sound pressure levels, but the sequence is in practice still just audible as it produces a higher pitched sound than the background noise (e.g. compressor pump) in the scan room. These measurement are comparable to those reported by Alibek et al., who measured a non-significant increase of 0.07 dB between RUFIS and ambient noise levels [31]. Costagli et al. measured an increase of 2.5dBA for RUFIS compared to ambient noise levels, however, the ambient noise level in their scan room was 52.7 dBA which is much

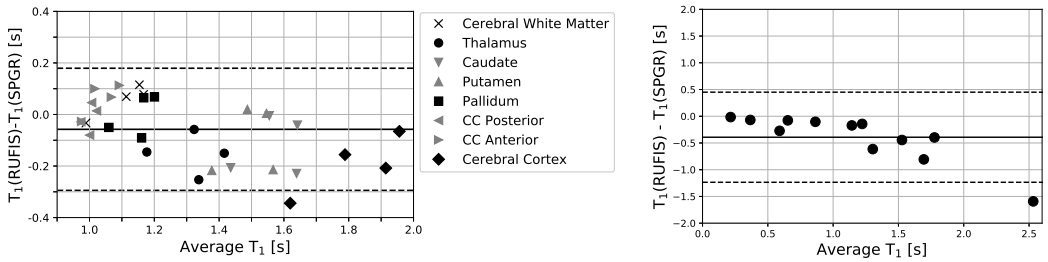

(A) - In vivo **(B) - Phantom**

FIGURE 6 Bland Altman analysis comparing RUFIS and SPGR in vivo **(A)**, and in the EUROSPIN quantitative phantom **(B)**. Both in vivo and phantom experiment showed lower T_1 estimates from RUFIS for longer T_1. Data is from first scan at first visit for both in vivo and phantom data.

lower than what we measured [9]. The increased acoustic noise during the SIMBA acquisition is due to the spoiling gradients after the preparation module.

4 | DISCUSSION

4.1 | Silent T_1-mapping

The acoustic noise produced by the MRI scanner during data acquisition is commonly reported by patients as one of the main unpleasant features of the scanning experience [32, 33]. In this work we have shown that the silent RUFIS sequence can be used for T_1-mapping together with a novel, silent, B_1^+ mapping method, SIMBA. We compared RUFIS to Cartesian SPGR and found that the two sequences produced comparable T_1 maps. The agreement between the two sequences was best in white matter, while in gray matter a longer T_1 was observed with SPGR. These results were also reflected in our phantom experiment. We found comparable in vivo repeatability between the two sequences, but reproducibility was better for RUFIS.

With no previous studies using RUFIS for VFA T_1 mapping, we can only compare our results to literature using non-ZTE acquisitions. Quantitatively, our T_1-values compares well with previous literature such as Stanisz et al. reporting T_1=1084 ± 45/1820 ± 114 in WM/GM[34]. In terms of reproducibility, our results also align with previous studies. Deoni et al. reported whole brain, voxel wise, intra-site CoV from SPGR VFA T_1-mapping of 6.4 [35]. Similar results were presented by Weiskopf et al. using VFA, reporting R_1 intra-site CoV of 3.9 and 4.7 in the corpus callosum and caudate nucleus repspectively[36]. However, the small sample size (N=4) and only two visits limit the conclusions that can be drawn from the current study.

There are several differences in the data acquisition between the two sequences that could contribute to the observed difference in T_1. The signal equation used assumes full spoiling of the transverse magnetisation. For SPGR, spoiling was achieved by RF and separate gradient spoiling after the readout. In RUFIS, spoiling was mainly achieved using RF spoiling, together with some gradient spoiling from the readout gradients. Previous work by Deichmann et al. showed that corrections for insufficient spoiling can be applied to improve T_1 reproducibility across different scan protocols [37], and it is therefore possible that some of the variability in T_1 between RUFIS can be attributed to the different spoiling behaviour. However, the algorithm used by Deichmann et al. assumed gradient spoiling along one axis after the readout, which does not apply for RUFIS. Furthermore, previous studies of spoiling behaviour in radial gradient

TABLE 1 T_1 values in isolated ROIs averaged between the two scans in the first visit together with within session repeatability estimates (CoR_w) from the first visit and between sessions reproducibility measurements (CoR_b). Lower values of CoR are better

	RUFIS			SPGR		
ROI	T_1[s]	$CoR_{w,1}$	CoR_b	T_1[s]	$CoR_{w,1}$	CoR_b
Cerebral WM	1.13±0.09	0.07	0.07	1.08±0.04	0.01	0.08
Thalamus	1.23±0.09	0.05	0.05	1.38±0.08	0.09	0.2
Caudate	1.5±0.1	0.06	0.09	1.63±0.08	0.05	0.2
Putamen	1.4±0.1	0.05	0.05	1.55±0.08	0.04	0.2
Pallidum	1.15±0.07	0.04	0.04	1.16±0.04	0.02	0.1
CC Posterior	0.99±0.03	0.05	0.05	1.01±0.03	0.04	0.1
CC Anterior	1.07±0.06	0.06	0.04	1.01±0.03	0.08	0.1
Cerebral Cortex	1.7±0.2	0.1	0.1	1.92±0.08	0.04	0.2
Mean	-	0.06	0.07	-	0.05	0.2

TABLE 2 Summary of acoustic noise measurements from each sequence. Values are reported as mean±σ noise levels over a 40 s period. The large standard deviation in the noise levels for SIMBA is due to the periodic spoiling gradients. (LAEQ - A-weighted equivalent continuous sound level, LCPEAK - C-weighted peak sound level)

Sequence	LAEQ [dBA]	LCPEAK [dBC]
Ambient	70.0 ± 0.2	89.7 ± 0.7
RUFIS	70.0 ± 0.2	89.6 ± 0.7
SIMBA	75.2 ± 4.0	102.5 ± 9.5
SPGR	103.3 ± 0.04	116.2 ± 0.1
Bloch-Siegert	98.8 ± 0.04	111.0 ± 0.1

echo sequences suggests that random RF spoiling increment and gradient moments can produce ideal spoiling [38, 39]. Corrections for insufficient spoiling in RUFIS will require modelling of spoiling along all three axes, which will be the focus of future work.

Another difference between the two sequences is the RF pulses for excitation: RUFIS used hard pulses, while SPGR used shaped pulses used for slab-selective excitation. Differences in pulse shape, and flip angles, between RUFIS and SPGR could contribute to magnetisation transfer effects, which have been shown to affect T_1 measurements [40]. The excitation profile in RUFIS was corrected for using a first order correction. However, as the readout direction changes for each spoke, the effective flip angle at any point in space, except isocentre, will change over time. A first order correction will make the effective flip angle equal to the average flip angle over time, and thus spin history effects are neglected. The lower average B_1^+ efficiency and stronger effect of the excitation profile around the edges of the brain could contribute to the difference in T_1 in cortical GM between the two sequence. However, we also see a difference in T_1 in deep GM structures, suggesting a non-spatial phenomenon.

Methods for reducing the acoustic noise in MRI scanning, can broadly be categorised as; hardware modifications [41, 42] or pulse sequence modifications, mainly through soft gradient pulses [43, 44, 45, 46]. In contrast, the silent

properties of RUFIS arise naturally from the gradient ordering of the sequence, and so performance is not compromised. Previous studies have used RUFIS for silent imaging including T_2-prepared fMRI [47], and structural imaging at 3T [31] and 7T [9]. Another silent ZTE sequence is Looping Star which uses gradient echoes for T_2^* weighted imaging [48]. Our acoustic noise measurement showed no measurable increase in the sound pressure levels during RUFIS scanning compared to background noise levels, similar to Alibek et al. [31]. However, the quoted decibel values will differ depending on the scan room environment and are not necessarily what the subject would experience inside the scanner. The acoustic noise will also change depending on scan parameters such as the TR and number of spokes. Nevertheless, we do not envisage any greater acoustic disturbance than measured herein.

We chose to use a relatively low readout bandwidth (7.8 kHz) for the RUFIS acquisition in this study as our sequence optimisation showed that this would enable the most optimal VFA flip angle sampling scheme. However, lower bandwidth will widen the point spread function and increase chemical shift artefacts [49]. In a 3D radial acquisition, chemical shift artefacts manifest in three dimensions as a spherical artefact. The chemical shift does not appear to be a major issue in our study at 3T, but translating this technique to higher field strength will require higher readout bandwidth.

4.2 | Silent B_1^+ mapping

T_1 mapping using VFA is inherently sensitive to errors in the B_1^+ map estimation. As shown by equation (2), and previously by other authors, the apparent T_1 scales with the square of the flip angle bias field [13, 14]. In this study, we chose to compare two complete protocols for T_1 mapping including B_1^+ mapping. We chose to use the Bloch-Siegert method for B_1^+ correction of the Cartesian SPGR data, as it is a standard sequence on the GE platform. This is not a silent sequence, however, and therefore we developed a new method for silent B_1^+ mapping (SIMBA), specifically designed for correction of RUFIS data. A train of hard RF pulses was used for magnetisation saturation to match the RUFIS acquisition as closely as possible. SIMBA could also be used with a single saturation pulse with different flip angles to match the excitation pulse in other sequences as well.

Comparison of the two B_1^+ mapping techniques revealed overall lower B_1^+ with SIMBA than Bloch-Siegert. Processing RUFIS VFA data with both B_1^+ techniques, figure 3, showed that the difference between the two techniques results in a global uniform scaling of the T_1 values towards lower T_1 with Bloch-Siegert. Our comparison of T_1 values between SPGR and RUFIS showed longer T_1 in GM with Bloch-Siegert corrected SPGR data compared to SIMBA corrected RUFIS. Using Bloch-Siegert with RUFIS would therefore increase the difference between the sequences. It is therefore unlikely that the observed differences in T_1 between the two sequences is caused by the B_1^+ map.

4.3 | Zero TE effects

One aspect of the RUFIS sequence that has not been studied in this work is the zero echo time (ZTE) readout, which results in sensitivity to short T_2 components, otherwise invisible to MR acquisitions [11, 12]. The ZTE effects can be observed in the T_1 and PD maps obtained with RUFIS, where a much higher proton density and better T_1 fit was observed in the cortical bone which has a very short T_1 and T_2, see white arrows in figure 4. Recent works have suggested that the ultra short T_2 component from the myelin lipids are visible using ZTE and ultra short TE (UTE) acquisitions [50, 51]. However, the low bandwidth used in this work means that the signal from the solid myelin components will decay within the first few samples, and would, if anything, only contribute to an increased point spread function. Therefore, it is unlikely that the ZTE properties of RUFIS contribute to the observed differences in T_1 between RUFIS and SPGR.

5 | CONCLUSIONS

T_1 mapping with the VFA method using spoiled gradient echo imaging (SPGR) is a highly efficient method for T_1 mapping but requires an additional B_1^+ map for correction of the B_1^+ field. RUFIS is a zero TE, silent imaging sequence with a spoiled free induction decay (FID) readout which effectively can be used for quantitative imaging using the same signal equations as SPGR. In this work we have shown that RUFIS can be used for silent VFA T_1 mapping with results that are very similar to a conventional Cartesian SPGR acquisition. A novel silent B_1^+ mapping technique based on RUFIS was also presented which can provide the necessary B_1^+ correction for VFA T_1 mapping using RUFIS.

We demonstrated a fully silent VFA T_1 and B_1^+ mapping protocol with higher reproducibility and comparable repeatability compared to the equivalent standard Cartesian SPGR sequence. Adoption of this protocol could lead to increased patient comfort in quantitative imaging studies.

ACKNOWLEDGEMENTS

This paper represents independent research part funded by the National Institute for Health Research (NIHR)-Wellcome Trust King's Clinical Research Facility and the NIHR Biomedical Research Centre at South London and Maudsley NHS Foundation Trust and King's College London. Emil Ljungberg is in receipt of a PhD studentship jointly funded by General Electric (GE) Healthcare and the NIHR Biomedical Research Centre at South London and Maudsley NHS Foundation Trust and King's College London. The views expressed are those of the author and not necessarily those of the NHS, the NIHR or the Department of Health and Social Care. This work was aslo supported by the Wellcome/EPSRC Centre for Medical Engineering [WT 203148/Z/16/Z]. The data presented in this study may be accessed by contacting the authors directly.

APPENDIX

5.1 | Derivation of the quantitative RUFIS signal equation

We begin from the results derived by Hsu and Lowe[52]. Let the longitudinal magnetisation of spoke n in segment m be $M_z(n, m)$. With N spokes per segment we get

$$M_z(n, m) = M_z(0, m) \cdot \cos^n(\alpha) E_1^n + \rho(1 - E_1) \cdot \frac{1 - \cos^n(\alpha) E_1^n}{1 - \cos(\alpha) E_1} \tag{9}$$

where $E_1 = e^{-TR/T_1}$, α is the excitation flip angle, and ρ is the proton density. If $n \to \infty$ then $\cos^n(\alpha) \to 0$, and (9) approaches the well known gradient echo steady state signal equation

$$\lim_{n\to\infty} M_z(n, m) = \rho \cdot \frac{1 - E_1}{1 - \cos(\alpha) E_1} = M_{z,spgr} \tag{10}$$

To simplify (9), we set $\xi = \cos(\alpha) E_1$ and substitute in $M_{z,spgr}$ to obtain

$$M_z(n, m) = M_z(0, m) \cdot \xi^n + M_{z,spgr} \cdot (1 - \xi^n). \tag{11}$$

With a segment of N spokes, the acquired magnetisation is proportional the average available longitudinal magnetisation of all spokes. This can be formulated as

$$\bar{M_z}(m) = \frac{1}{N} \sum_{i=0}^{N-1} M_z(i, m) = \frac{1}{N} \sum_{i=0}^{N-1} \left(M_z(0, m) \cdot \xi^i + M_{z,spgr} \cdot (1 - \xi^i) \right) = M_z(0, m) \cdot f + M_{z,spgr}(1 - f) \tag{12}$$

where

$$f = \frac{1}{N} \sum_{i=0}^{N-1} \xi^i = \frac{1}{N} \frac{1 - \xi^N}{1 - \xi} = \frac{1}{N} \frac{1 - (\cos\alpha \cdot e^{-TR/T_1})^N}{1 - \cos\alpha \cdot e^{-TR/T_1}}. \tag{13}$$

Index runs from 0 to $N - 1$ as the acquired magnetisation is proportional to available magnetisation before each spoke.

When data is collected in a steady state, the inter-segment delay (τ) will cause intermittent T_1 recovery. The effect of this will depend on the number of spokes per segment as well as τ. The effect of this delay can be calculated analytically. The magnetisation at the beginning of segment $m + 1$ is proportional to the magnetisation at the end of the previous segment as well as the T_1 recovery between segments as

$$M_z(0, m + 1) = M_z(N, m) \cdot e^{-\tau/T_1} + \rho(1 - e^{-\tau/T_1}). \tag{14}$$

Combining (14) with (11) yields

$$M_z(0, m + 1) = \left[M_z(0, m) \cdot \xi^N + M_{z,spgr} \cdot (1 - \xi^N) \right] e^{-\tau/T_1} + \rho(1 - e^{-\tau/T_1}). \tag{15}$$

If the magnetisation at the beginning of each segment has reached a steady state ($\tilde{M}_0$) we can substitute $M_z(0, m + 1)$

and $M_z(0, m)$ with $\tilde{M}_0$ in (15) and solving for $\tilde{M}_0$ to get

$$\tilde{M}_0 = M_{z,spgr} \cdot \frac{e^{-\tau/T_1}(1-\xi^N)}{1-\xi^N e^{-\tau/T_1}} + \rho \frac{1-e^{-\tau/T_1}}{1-\xi^N e^{-\tau/T_1}}. \quad (16)$$

SUPPORTING INFORMATION

Table S1 Within the first visit and between sessions coefficient of variation (CoV_w / CoV_b) for RUFIS and SPGR T_1 measurements. Lower values indicate higher repeatability and reproducibility. Values reported as mean$\pm\sigma$.

REFERENCES

[1] Christensen KA, Grant DM, Schulman EM, Walling C. Optimal determination of relaxation times of fourier transform nuclear magnetic resonance. Determination of spin-lattice relaxation times in chemically polarized species. The Journal of Physical Chemistry 1974;78(19):1971–1977. http://pubs.acs.org/doi/abs/10.1021/j100612a022.

[2] Gupta RK. A new look at the method of variable nutation angle for the measurement of spin-lattice relaxation times using fourier transform NMR. Journal of Magnetic Resonance 1977;25(1):231–235.

[3] Homer J, Beevers MS. Driven-equilibrium single-pulse observation of T1 relaxation. A reevaluation of a rapid "new" method for determining NMR spin-lattice relaxation times. Journal of Magnetic Resonance (1969) 1985;63(2):287–297.

[4] Fram EK, Herfkens RJ, Johnson GA, Glover GH, Karis JP, Shimakawa A, et al. Rapid calculation of T1 using variable flip angle gradient refocused imaging. Magnetic Resonance Imaging 1987;5(3):201–208.

[5] Deoni SCL. High-Resolution T1 Mapping of the Brain at 3T with Driven Equilibrium Single Pulse Observation of T1 with High-Speed Incorporation of RF Field Inhomogeneities (DESPOT1-HIFI). Journal of Magnetic Resonance Imaging 2007;26:1106–1111.

[6] Wang HZ, Riederer SJ, Lee JN. Optimizing the precision in T1 relaxation estimation using limited flip angles. Magnetic Resonance in Medicine 1987;5(5):399–416.

[7] Deoni SCL, Rutt BK, Peters TM. Rapid combined T1 and T2 mapping using gradient recalled acquisition in the steady state. Magnetic Resonance in Medicine 2003;49(3):515–526.

[8] Madio DP, Lowe IJ. Ultra-Fast Imaging Using Low Flip Angles and FIDs. Magnetic resonance in medicine 1995;34(4):525–529.

[9] Costagli M, Symms MR, Angeli L, Kelley DAC, Biagi L, Farnetani A, et al. Assessment of Silent T1-weighted head imaging at 7 T. European Radiology 2016;26(6):1879–1888. http://dx.doi.org/10.1007/s00330-015-3954-2.

[10] Weiger M, Pruessmann KP. MRI with Zero Echo Time. eMagRes 2012;1:311–322.

[11] Wiesinger F, Sacolick LI, Menini A, Kaushik SS, Ahn S, Veit-Haibach P, et al. Zero TE MR bone imaging in the head. Magnetic Resonance in Medicine 2016;75(1):107–114.

[12] Gibiino F, Sacolick L, Menini A, Landini L, Wiesinger F. Free-breathing, zero-TE MR lung imaging. Magnetic Resonance Materials in Physics, Biology and Medicine 2015;28:207–215. http://dx.doi.org/10.1007/s10334-014-0459-y.

[13] Helms G, Dathe H, Dechent P. Quantitative FLASH MRI at 3T using a rational approximation of the Ernst equation. Magnetic Resonance in Medicine 2008;59(3):667–672.

[14] Baudrexel S, Reitz SC, Hof S, Gracien RM, Fleischer V, Zimmermann H, et al. Quantitative T1 and proton density mapping with direct calculation of radiofrequency coil transmit and receive profiles from two-point variable flip angle data. NMR in Biomedicine 2016;29(3):349–360.

[15] Grodzki DM, Jakob PM, Heismann B. Correcting slice selectivity in hard pulse sequences. Journal of Magnetic Resonance 2012;214:61–67. http://dx.doi.org/10.1016/j.jmr.2011.10.005.

[16] Wood TC. Improved formulas for the two optimum VFA flip-angles. Magnetic Resonance in Medicine 2015;74(1):1–3.

[17] Sacolick LI, Wiesinger F, Hancu I, Vogel MW. B1 mapping by Bloch-Siegert shift. Magnetic Resonance in Medicine 2010;63(5):1315–1322.

[18] Lerski RA, de Certaines JD. II. Performance assessment and quality control in MRI by Eurospin test objects and protocols. Magnetic Resonance Imaging 1993;11(6):817–833.

[19] Uecker M, Lai P, Murphy MJ, Virtue P, Elad M, Pauly JM, et al. ESPIRiT - An eigenvalue approach to autocalibrating parallel MRI: Where SENSE meets GRAPPA. Magnetic Resonance in Medicine 2014;71(3):990–1001.

[20] Uecker M, Tamir JI, BART Toolbox for Computational Magnetic Resonance Imaging; 2017. https://doi.org/10.5281/zenodo.1066014.

[21] Tamir J, Ong F, Cheng JY, Uecker M, Lustig M. Generalized Magnetic Resonance Image Reconstruction using The Berkeley Advanced Reconstruction Toolbox. In: ISMRM Workshop on Data Sampling and Image Reconstruction Sedona; 2016. .

[22] McKenzie CA, Yeh EN, Ohliger MA, Price MD, Sodickson DK. Self-calibrating parallel imaging with automatic coil sensitivity extraction. Magnetic Resonance in Medicine 2002;47(3):529–538.

[23] Jenkinson M, Bannister P, Brady M, Smith S. Improved optimization for the robust and accurate linear registration and motion correction of brain images. NeuroImage 2002;17(2):825–841.

[24] Avants BB, Tustison NJ, Song G, Cook PA, Klein A, Gee JC. A reproducible evaluation of ANTs similarity metric performance in brain image registration. NeuroImage 2011 feb;54(3):2033–2044.

[25] Wood TC. QUIT: QUantitative Imaging Tools. Journal of Open Source Software 2017;3(26):656. https://github.com/spinicist/QUIT.

[26] Avants BB, Epstein CL, Grossman M, Gee JC. Symmetric diffeomorphic image registration with cross-correlation: Evaluating automated labeling of elderly and neurodegenerative brain. Medical Image Analysis 2008;12(1):26–41.

[27] Fischl B, Salat DH, Busa E, Albert M, Dieterich M, Haselgrove C, et al. Whole Brain Segmentation: Automated Labeling of Neuroanatomical Structures in the Human Brain. Neuron 2002;33(3):341–355.

[28] Gorgolewski K, Burns CD, Madison C, Clark D, Halchenko YO, Waskom ML, et al. Nipype: A Flexible, Lightweight and Extensible Neuroimaging Data Processing Framework in Python. Frontiers in Neuroinformatics 2011;5(August). http://journal.frontiersin.org/article/10.3389/fninf.2011.00013/abstract.

[29] Sullivan DC, Obuchowski NA, Kessler LG, Raunig DL, Gatsonis C, Huang EP, et al. Metrology Standards for Quantitative Imaging Biomarkers. Radiology 2015;277(3):813–825. http://pubs.rsna.org/doi/10.1148/radiol.2015142202.

[30] Bland JM, Altman DG. Statistical Methods for Assessing Agreement Between Two Methods of Clinical Measurement. Lancet 1986;327:307–310. http://www.sciencedirect.com/science/article/pii/S0140673686908378.

[31] Alibek S, Vogel M, Sun W, Winkler D, Baker CA, Burke M, et al. Acoustic noise reduction in MRI using Silent Scan: An initial experience. Diagnostic and Interventional Radiology 2014;20(4):360–363.

[32] MacKenzie R, Sims C, Owens RG, Dixon AK. Patients' perceptions of magnetic resonance imaging. Clinical radiology 1995;50(3):137–143.

[33] McNulty JP, McNulty S. Acoustic noise in magnetic resonance imaging: An ongoing issue. Radiography 2009;15(4):320–326. http://dx.doi.org/10.1016/j.radi.2009.01.001.

[34] Stanisz GJ, Odrobina EE, Pun J, Escaravage M, Graham SJ, Bronskill MJ, et al. T1, T2 relaxation and magnetization transfer in tissue at 3T. Magnetic Resonance in Medicine 2005;54(3):507–512.

[35] Deoni SCL, Williams SCR, Jezzard P, Suckling J, Murphy DGM, Jones DK. Standardized structural magnetic resonance imaging in multicentre studies using quantitative T1 and T2 imaging at 1.5T. NeuroImage 2008;40:662–671.

[36] Weiskopf N, Suckling J, Williams G, Correia MM, Inkster B, Tait R, et al. Quantitative multi-parameter mapping of R1, PD*, MT, and R2* at 3T: a multi-center validation. Frontiers in Neuroscience 2013;7(95):1–11.

[37] Deichmann R, Baudrexel S, Ulrike N. T1 Mapping With the Variable Flip Angle Technique: A Simple Correction for Insufficient Spoiling of Transverse Magnetization. Magnetic Resonance in Medicine 2018;79:3082–3092.

[38] Wei L, Hee KS. Improved signal spoiling in fast radial gradient-echo imaging: Applied to accurate t1 mapping and flip angle correction. Magnetic Resonance in Medicine 2009;62(5):1185–1194.

[39] Roeloffs V, Voit D, Frahm J. Spoiling without additional gradients: Radial FLASH MRI with randomized radiofrequency phases. Magnetic Resonance in Medicine 2016;75(5):2094–2099.

[40] Rui RP, Malik SJ, Hajnal JV. Fast quantitative MRI using controlled saturation magnetization transfer. Magnetic Resonance in Medicine 2019;81(2):907–920.

[41] Mansfield P, Glover PM, Beaumont J. Sound generation in gradient coil structures for MRI. Magnetic resonance in medicine : official journal of the Society of Magnetic Resonance in Medicine / Society of Magnetic Resonance in Medicine 1998;39(4):539–50. http://www.ncbi.nlm.nih.gov/pubmed/9543415.

[42] Edelstein Wa, Hedeen Ra, Mallozzi RP, El-Hamamsy SA, Ackermann Ra, Havens TJ. Making MRI quieter. Magnetic Resonance Imaging 2002;20:155–163.

[43] Hennel F, Girard F, Loenneker T. "Silent" MRI with soft gradient pulses. Magnetic Resonance in Medicine 1999;42:6–10. http://www.ncbi.nlm.nih.gov/pubmed/10398943.

[44] Hennel F. Fast spin echo and fast gradient echo MRI with low acoustic noise. Journal of magnetic resonance imaging : JMRI 2001;13(6):960–6. http://www.ncbi.nlm.nih.gov/pubmed/11382960.

[45] Schmitter S, Diesch E, Amann M, Kroll a, Moayer M, Schad LR. Silent echo-planar imaging for auditory FMRI. Magnetic Resonance Materials in Physics, Biology and Medicine 2008;21(5):317–325. http://www.ncbi.nlm.nih.gov/pubmed/18716815.

[46] Segbers M, Rizzo Sierra CV, Duifhuis H, Hoogduin JM. Shaping and timing gradient pulses to reduce MRI acoustic noise. Magnetic Resonance in Medicine 2010;64(2):546–53. http://www.ncbi.nlm.nih.gov/pubmed/20665798.

[47] Solana AB, Menini A, Sacolick LI, Hehn N, Wiesinger F. Quiet and Distortion-Free , Whole Brain BOLD fMRI Using T2 -Prepared RUFIS. Magnetic Resonance in Medicine 2016;75:1402–1412.

[48] Wiesinger F, Menini A, Solana AB. Looping Star. Magnetic Resonance in Medicine 2018;0(0):1–12.

[49] Bydder M, Du J, Takahashi A, Shimakawa A, Hamilton G, Sinha S, et al. Chemical Shift Artifact in Center-Out Radial Sampling: A Potential Pitfall in Clinical Diagnosis. In: Proc. Intl. Soc. Mag. Reson. Med 15; 2007. p. 1811.

[50] Du J, Sheth V, He Q, Carl M, Chen J, Corey-bloom J, et al. Measurement of T1 of the Ultrashort T2* Components in White Matter of the Brain at 3T. PLoS ONE 2014;9(8).

[51] Boucneau T, Cao P, Tang S, Han M, Xu D, Henry RG, et al. In vivo characterization of brain ultrashort-T2 components. Magnetic Resonance in Medicine 2017;00(November):1–10. http://doi.wiley.com/10.1002/mrm.27037.

[52] Hsu JJ, Lowe IJ. Spin-lattice relaxation and a fast T1-map acquisition method in MRI with transient-state magnetization. Journal of Magnetic Resonance 2004;169(2):270–278.

SUPPORTING INFORMATION

TABLE S1 Within the first visit and between sessions coefficient of variation (CoV_w / CoV_b) for RUFIS and SPGR T_1 measurements. Lower values indicate higher repeatability and reproducibility. Values reported as mean±σ.

	RUFIS		SPGR	
ROI	$CoV_{w,1}$	CoV_b	$CoV_{w,1}$	CoV_b
Cerebral WM	1.8±0.9	3 ±2	0.7±0.4	2 ±1
Thalamus	1.2±0.7	1.6±0.6	2 ±1	5 ±4
Caudate	1.2±0.7	1.9±0.4	1.0±0.4	5 ±3
Putamen	1.0±0.6	1.1±0.5	0.9±0.7	5 ±4
Pallidum	1.1±0.7	1.0±0.2	1.3±0.7	4 ±3
CC Posterior	1.5±0.9	1.2±0.4	2 ±1	4 ±2
CC Anterior	1.7±0.7	0.5±0.4	2 ±1	3 ±3
Cerebral Cortex	2 ±1	3 ±2	0.9±0.5	3 ±2
Mean	1.5±0.4	1.6±0.8	1.4±0.	4 ±1